

See discussions, stats, and author profiles for this publication at: <https://www.researchgate.net/publication/241690126>

Ion Transport in a pH-Regulated Nanopore

ARTICLE in ANALYTICAL CHEMISTRY · JUNE 2013

Impact Factor: 5.64 · DOI: 10.1021/ac401536g · Source: PubMed

CITATIONS

32

READS

80

3 AUTHORS:



Li-Hsien Yeh

National Yunlin University of Science and Tec...

63 PUBLICATIONS 717 CITATIONS

SEE PROFILE



Mingkan Zhang

Oak Ridge National Laboratory

16 PUBLICATIONS 272 CITATIONS

SEE PROFILE



Shizhi Qian

Old Dominion University

156 PUBLICATIONS 2,513 CITATIONS

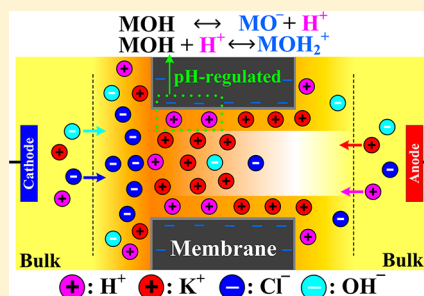
SEE PROFILE

Ion Transport in a pH-Regulated Nanopore

Li-Hsien Yeh,^{*,†} Mingkan Zhang,[‡] and Shizhi Qian^{*,§}[†]Department of Chemical and Materials Engineering, National Yunlin University of Science and Technology, Yunlin 64002, Taiwan[‡]Department of Geology and Geophysics, University of Wyoming, Laramie, Wyoming 82071, United States[§]Institute of Micro/Nanotechnology, Old Dominion University, Norfolk, Virginia 23529, United States

S Supporting Information

ABSTRACT: Fundamental understanding of ion transport phenomena in nanopores is crucial for designing the next-generation nanofluidic devices. Due to surface reactions of dissociable functional groups on the nanopore wall, the surface charge density highly depends upon the proton concentration on the nanopore wall, which in turn affects the electrokinetic transport of ions, fluid, and particles within the nanopore. Electrokinetic ion transport in a pH-regulated nanopore, taking into account both multiple ionic species and charge regulation on the nanopore wall, is theoretically investigated for the first time. The model is verified by the experimental data of nanopore conductance available in the literature. The results demonstrate that the spatial distribution of the surface charge density at the nanopore wall and the resulting ion transport phenomena, such as ion concentration polarization (ICP), ion selectivity, and conductance, are significantly affected by the background solution properties, such as the pH and salt concentration.



Synthetic nanopores have attracted growing scientific interest due to their potential applications ranging from biosensing to control of molecular transport.^{1–9} In the nanopore sensing techniques, physicochemical properties of (bio)nanoparticles^{9–13} and nanopores¹⁴ can be probed through discriminating the characteristic temporary changes in the ionic current signal by translocation of individual particles through a nanopore. An electric double layer (EDL) forms in the vicinity of the charged nanopore wall in contact with an aqueous solution. It is generally recognized that the overlapping of EDLs in these nanofluidic devices is significant, resulting in several unique features, such as ion selectivity,^{15,16} ionic current rectification (ICR),^{17–21} and ion concentration polarization (ICP).^{22–24} Numerous results have demonstrated that these ion transport phenomena play a crucial role in the analysis of the ionic current signals in nanopore-based biosensing^{25–29} and have potential applications in regulation of ion transport^{30–32} and separation of (bio)entities.²⁴ These results suggest that a comprehensive understanding of the electrokinetic ion transport in a nanopore is highly desirable for the development of the next-generation nanofluidic devices.

Several theoretical efforts have been made to model electrokinetic ion transport in a nanopore or nanochannel using the Poisson–Nernst–Planck (PNP) equations.^{16,23,33–42} For example, Daiguji et al.³³ investigated ion transport in a silica nanochannel embedded with a gate electrode in its middle region without considering the effect of electroosmotic flow (EOF) within the charged nanochannel. They found that the ion transport phenomena can be significantly affected by the surface charge density of the nanochannel, tuned by the gate potential applied to the gate electrode. On the basis of this analysis, ion transport and ICR in cylindrical and conical

nanopores were further analyzed by several investigators.^{34–36} Those analyses were extended by Vlassiuk et al.¹⁶ to take into account the EOF effect on the ion selectivity in a cylindrical nanochannel. They concluded that the contribution of electroosmosis becomes noticeable especially if the surface charge density of the nanochannel/nanopore is sufficiently high. A similar conclusion was drawn by Ai et al.,³⁷ who investigated the ICR in a conical nanopore by a continuum-based model, comprising the PNP and Navier–Stokes equations. On the basis of the same model, Ai et al.,³⁸ Zhang et al.,³⁹ Yeh et al.,^{23,42} and Singh and Kumar^{40,41} further investigated ion transport and ICR in various types of nanopores.

The previous analyses based on the PNP equations assumed that the surface charge density of the nanopore/nanochannel wall remains constant and only considered cations and anions dissociated from the background salt. However, it is well-known that the substrate material of solid-state nanopores, such as silicon dioxide (SiO₂) and silicon nitride (Si₃N₄), in contact with an aqueous solution typically reveals a charge-regulated nature due to the protonation/deprotonation surface reactions.^{43–47} This implies that the surface charge property of the nanopore wall, which significantly affects the electrokinetic ion transport within the nanopore, depends strongly on the local concentration of the hydrogen ions on its surface. Previous studies on the ion and fluid transport in a charge-regulated nanopore/nanochannel used the Poisson–Boltzmann (PB)

Received: May 22, 2013

Accepted: June 21, 2013

Published: June 21, 2013

equation based on the assumption of an equilibrium EDL,^{43–48} where the ionic concentrations near the charged surface follow the Boltzmann distribution. Many experimental and theoretical results have shown that ion selectivity and ICP phenomena inside nanofluidic devices are significant,^{15,16,22,31} resulting in an axial ionic concentration gradient, the so-called diffusion boundary layer (DBL),¹⁵ as schematically depicted in Figure 1. Therefore, the PB model with an undistorted EDL is not appropriate in the nanopore-based systems with dimensions comparable to the EDL thickness.

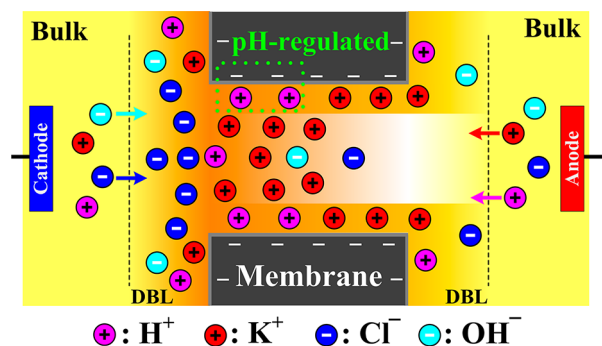


Figure 1. Schematic illustration of the selective ion transport in a pH-regulated nanopore containing multiple ionic species, H^+ , K^+ , Cl^- , and OH^- . ICP occurs at the micro/nanofluidic interfaces, and therefore, both cations and anions are enriched (depleted) at the cathode (anode) side of the nanopore.

Considering the fast growth in widespread applications of the nanofluidic devices, we investigate, for the first time, the electrokinetic ion transport in a pH-regulated nanopore containing multiple ionic species. In contrast to the previous studies using the PB model,^{43–48} the model consists of the multi-ion PNP equations for the ionic mass transport and Navier–Stokes equations for the flow field. Different from the existing studies where the PNP and Navier–Stokes equations with a prescribed constant surface charge density and only two ionic species dissociated from the background salt solution were considered,^{26,48} this study considered four ionic species, including H^+ , OH^- , and the two species dissociated from the background salt. In addition, the surface charge density of the nanopore wall is not prescribed and is calculated from the protonation/deprotonation of the silanol groups (SiOH) on the silica-based nanopore wall. The developed model is verified by comparing its prediction of nanopore conductance to the experimental data available in the literature. The results show that the spatial distribution of the surface charge density on the nanopore wall and the electrokinetic ion transport phenomena (e.g., ICP, local electric field, potential drop within the nanopore, nanopore conductance, and ion selectivity) depend strongly on the background solution properties, such as the pH and salt concentration.

THEORETICAL MODEL

We consider a cylindrical nanopore of length L_N and radius R_N connecting two large, identical fluid reservoirs filled with an electrolyte solution containing N types of ionic species, as schematically shown in Figure 1. The axial length, L_R , and radius, R_R , of the reservoirs are large enough so that the concentration of each ionic species at places far away from the nanopore maintains its bulk ionic concentration, C_{j0} ($j = 1, \dots, N$). To investigate the electrokinetic ion transport phenomena

in the nanopore, a potential bias, V_0 , is applied between two electrodes positioned far away from the nanopore inside the two fluid reservoirs. For simplicity, the Stern layer effect on the ion transport in the nanopore is neglected since the counterions inside the stern layer are rigidly immobile and do not contribute to the ionic current.^{16,33} Due to the axial symmetry, the cylindrical coordinate system (r, z) with the origin at the center of the nanopore is adopted in this study.

The following verified continuum-based model,^{16,28,42} taking into account multiple ionic species, is employed to describe the electrostatics, hydrodynamics, and ionic mass transport: (i) PNP equations for the electrical potential and the ionic mass transport

$$-\epsilon_f \nabla^2 V = \rho_e = F \sum_{j=1}^N z_j c_j \quad (1)$$

$$\nabla \cdot \mathbf{N}_j = \nabla \cdot \left(\mathbf{u} c_j - D_j \nabla c_j - z_j \frac{D_j}{RT} F c_j \nabla V \right) = 0 \quad (2)$$

$j = 1, 2, \dots, N$

Here, V is the electric potential, $\rho_e = F \sum_{j=1}^N z_j c_j$ is the space charge density of mobile ions, \mathbf{N}_j , c_j , D_j , and z_j are the flux density, concentration, diffusivity, and valence of the j th ionic species, respectively, ϵ_f , F , R , and T are the fluid permittivity, Faraday constant, universal gas constant, and absolute temperature, respectively, and $\mathbf{u} = u\mathbf{e}_r + v\mathbf{e}_z$ is the fluid velocity, with \mathbf{e}_r and \mathbf{e}_z being the unit vectors in the r - and z -directions, respectively. Note that the first, second, and third terms in the ionic flux density, \mathbf{N}_j , denote contributions from the convective, diffusive, and migrative fluxes, respectively. (ii) Navier–Stokes and continuity equations for the flow field

$$-\nabla p + \mu \nabla^2 \mathbf{u} - \rho_e \nabla V = \mathbf{0} \quad (3)$$

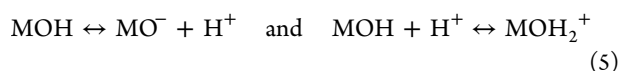
$$\nabla \cdot \mathbf{u} = 0 \quad (4)$$

where p and μ are the hydrodynamic pressure and the fluid viscosity, respectively. Since the Reynolds numbers of the EOF in nanofluidic devices are very small, the inertial terms in the Navier–Stokes equations can be safely neglected.

The following boundary conditions are applied to the above highly coupled governing eqs 1–4: (i) The ionic concentrations at the ends of the two reservoirs are maintained at their bulk values (i.e., $c_j = C_{j0}$), and the corresponding electric potentials are $V(\text{cathode}) = -V_0$ and $V(\text{anode}) = 0$. A normal flow with no external pressure gradient (i.e., $p = 0$) is specified at the ends of the reservoirs. (ii) The fixed membrane wall is nonslip and ion-impenetrable and bears a surface charge density, σ_w , yielding $\mathbf{u} = \mathbf{0}$, $\mathbf{n} \cdot \mathbf{N}_j = 0$, and $-\mathbf{n} \cdot \nabla V = \sigma_w / \epsilon_f$. Here \mathbf{n} is the unit outer normal vector. (iii) The slip boundary condition for the flow field, the insulation boundary condition for the potential ($-\mathbf{n} \cdot \nabla V = 0$), and zero normal ionic fluxes ($\mathbf{n} \cdot \mathbf{N}_j = 0$) are applied at the side boundaries of the two reservoirs, which are far away from the nanopore. (iv) The symmetric boundary condition is specified along the axis of the nanopore.

Note that σ_w is a prescribed constant in many existing studies^{16,31,33–41,48,49} and is part of the solution in the current study. Since the dielectric material of the membrane wall in contact with an aqueous solution reveals a charge-regulated nature, its surface charge density can be determined by the

following deprotonation/protonation reactions with equilibrium constants K_A and K_B :



In the above reactions, $10^{-\text{p}K_A} = \Gamma_{\text{MO}^-}[\text{H}^+]_s / \Gamma_{\text{MOH}}$ and $10^{-\text{p}K_B} = \Gamma_{\text{MOH}_2^+} / (\Gamma_{\text{MOH}}[\text{H}^+]_s)$, with $\text{p}K_j = -[\log K_j]$ ($j = A$ and B), Γ_{MOH} , Γ_{MO^-} , and $\Gamma_{\text{MOH}_2^+}$ are the surface site densities of MOH, MO^- , and MOH_2^+ , respectively, and $[\text{H}^+]_s$ is the molar concentration of H^+ ions at the membrane wall/liquid interface. The total number site density of dissociable MOH molecules on the membrane wall surface is $\Gamma_{\text{total}} = \Gamma_{\text{MOH}} + \Gamma_{\text{MO}^-} + \Gamma_{\text{MOH}_2^+}$. The surface charge density of the membrane wall can be expressed as

$$\begin{aligned} \sigma_w &= -F(\Gamma_{\text{MO}^-} - \Gamma_{\text{MOH}_2^+}) \\ &= -F\Gamma_{\text{total}} \left\{ \frac{10^{-\text{p}K_A} - 10^{-\text{p}K_B}([\text{H}^+]_s)^2}{10^{-\text{p}K_A} + [\text{H}^+]_s + 10^{-\text{p}K_B}([\text{H}^+]_s)^2} \right\} \quad (6) \end{aligned}$$

This expression suggests that σ_w depends not only on the physicochemical properties of the dielectric membrane material (Γ_{total} , $\text{p}K_A$, and $\text{p}K_B$) but also on the local pH ($= -[\log [\text{H}^+]_s] = -[\log(c_{1s}/1000)]$) on the membrane wall, where c_{1s} is the local molar concentration of H^+ ions at the membrane wall/liquid interface. Therefore, σ_w is not constant and homogeneous on the membrane wall, and previous studies using a prescribed constant surface charge density for different salt concentrations are not appropriate.^{16,31,33–41,48,49} For the silica-based nanopore/nanochannel, reported values for the parameters Γ_{total} , $\text{p}K_A$, and $\text{p}K_B$ are 3.8–8 nm⁻², 6.6–8, and 0–2, respectively.^{43,45,50}

The conductance of the nanopore, G , can be evaluated by

$$G = I/V_0 = \left[\int_S F \left(\sum_{j=1}^N z_j \mathbf{N}_j \right) \cdot \mathbf{n} \, dS \right] / V_0 \quad (7)$$

where I is the ionic current flowing through the nanopore and S denotes the surface of either the anode or cathode positioned at either end of the reservoirs. Note that the present model for describing the ion transport in a solid-state nanopore is more general and realistic than most of the previous ones due to the consideration of H^+ and OH^- ions dissociated from water and the surface chemistry reactions of the dielectric membrane material (charge regulation).

RESULTS AND DISCUSSION

The fully coupled model described above is numerically solved using the commercial finite-element package COMSOL (version 3.5a, www.comsol.com), operating in a high-performance cluster, which has been verified to be sufficiently efficient and accurate for solving similar electrokinetic ion transport problems where only cations and anions dissociated from the background salt are considered.^{23,37,42} A finer mesh is generated around the charged membrane wall to capture its EDL. Typically, the total number of the mesh is around 130 000. A more detailed description of the numerical implementation is available in the literature.^{42,51}

We assume that the background salt in the electrolyte solution is KCl of bulk concentration C_{KCl} , and its pH is adjusted by KOH and HCl. Therefore, four major ionic species (i.e., $N = 4$), H^+ , K^+ , Cl^- , and OH^- , are considered, and their

bulk concentrations are, respectively, C_{10} , C_{20} , C_{30} , and C_{40} (in units of millimolar). Due to electroneutrality, the following bulk concentrations for the species are applied: $C_{10} = 10^{-\text{pH}+3}$, $C_{20} = C_{\text{KCl}} + 10^{-\text{pH}+3} - 10^{-(14-\text{pH})+3}$, and $C_{40} = 10^{-(14-\text{pH})+3}$ for $\text{pH} \leq 7$ and $C_{10} = 10^{-\text{pH}+3}$, $C_{20} = C_{\text{KCl}} - 10^{-\text{pH}+3} + 10^{-(14-\text{pH})+3}$, $C_{30} = C_{\text{KCl}}$, and $C_{40} = 10^{-(14-\text{pH})+3}$ for $\text{pH} > 7$.⁵² Here, $\text{pH} = -[\log([\text{H}^+]_0)] = -[\log(C_{10}/1000)]$, with $[\text{H}^+]_0$ being the bulk molar concentration of H^+ ions. In the present study, the sizes of both reservoirs are $L_R = R_R = 200$ nm. The diffusivities for H^+ , K^+ , Cl^- , and OH^- ions are 9.31×10^{-9} , 1.96×10^{-9} , 2.03×10^{-9} , and 5.30×10^{-9} m²/s, respectively.⁵³ The other physical parameters used in the simulations are $\epsilon_f = 7.08 \times 10^{-10}$ F/m, $R = 8.31$ J/(K·mol), $F = 96490$ C/mol, $\mu = 1 \times 10^{-3}$ Pa·s, and $T = 300$ K.

Verification by Experimental Data. The applicability of the present theoretical model is first verified by the experimental data of Smeets et al.²⁶ on the conductance of a solid-state nanopore with $L_N = 34$ nm, $R_N = 5 \pm 1$ nm, $V_0 = 200$ mV, and a background solution pH of 7.5. Figure 2 shows the dependence of the nanopore conductance, G , on the background salt concentration, C_{KCl} .

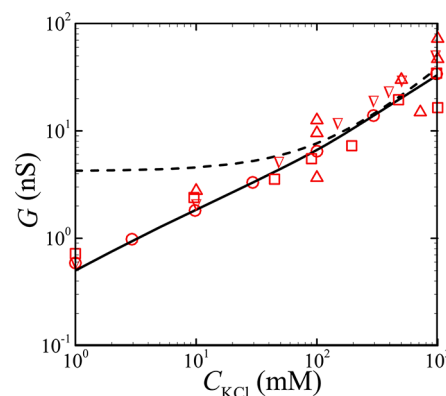


Figure 2. Conductance in a pH-regulated silica nanopore of length $L_N = 34$ nm as a function of the background salt concentration, C_{KCl} , at pH = 7.5: symbols, experimental data of Smeets et al.;²⁶ solid line, present numerical result at $R_N = 5.1$ nm, $\text{p}K_A = 7$, $\text{p}K_B = 1.9$, and $\Gamma_{\text{total}} = 4.8$ nm⁻²; dashed line, analytical result of eq 8 at the typical surface charge density of the silica nanopore, $\sigma_w = -60$ mC/m².⁴⁸

The dashed line in Figure 2 represents the following analytical result when only K^+ and Cl^- ions dissociated from the background salt KCl are considered:²⁶

$$G = \frac{\pi R_N^2}{L_N} \left[(\mu_2 + \mu_3) C_{\text{KCl}} F + \mu_2 \frac{2|\sigma_w|}{R_N} \right] \quad (8)$$

where $\mu_2(\text{K}^+) = 7.616 \times 10^{-8}$ m² s⁻¹ V⁻¹ and $\mu_3(\text{Cl}^-) = 7.909 \times 10^{-8}$ m² s⁻¹ V⁻¹. As shown in Figure 2, prediction of our model (solid line) using $R_N = 5.1$ nm, $\text{p}K_A = 7$, $\text{p}K_B = 1.9$, and $\Gamma_{\text{total}} = 4.8$ nm⁻² agrees very well with the experimental data (symbols). The fitted values of $\text{p}K_A$, $\text{p}K_B$, and Γ_{total} are also consistent with those reported in the literature.^{43,45,50} It is thus confirmed that the present model successfully captures the essential physics of the conductance in a silica nanopore with the consideration of the charge regulation nature. On the other hand, the analytical result of eq 8 (dashed line) based on a constant surface charge density, $\sigma_w = -60$ mC/m², a typical value of the silica nanopore used in the literature,^{26,48} is unable to describe the general trend of G , especially when the salt

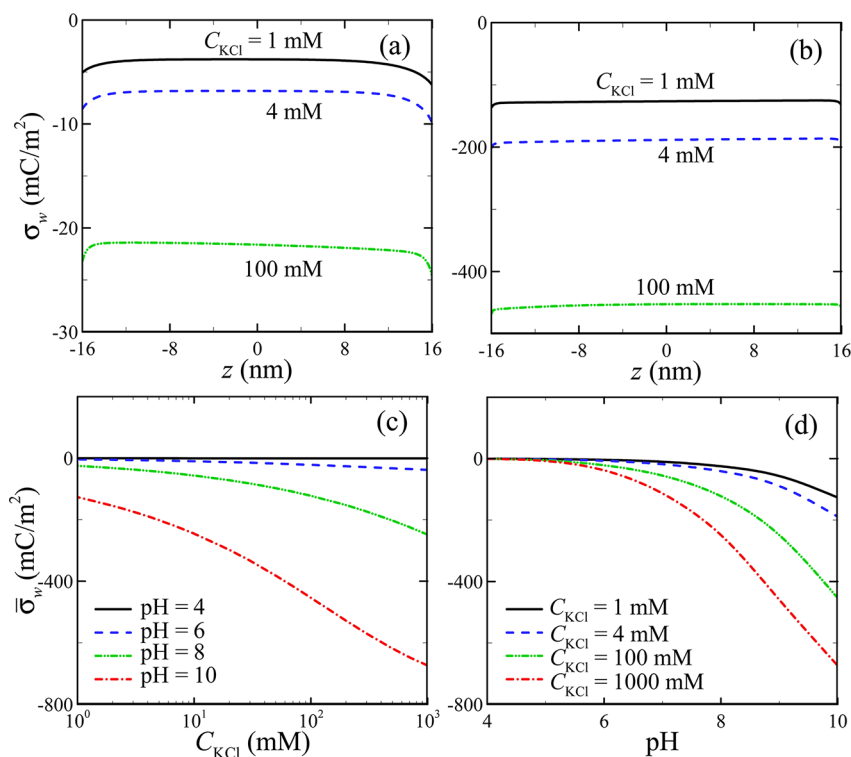


Figure 3. Surface charge density, σ_w , along the inner nanopore wall for various background salt concentrations, C_{KCl} , at pH = 6 (a) and 10 (b) and the surface-averaged charge density, $\bar{\sigma}_w$, as a function of C_{KCl} for various pH values (c) and as a function of pH for various C_{KCl} values (d).

concentration is relatively low. This is expected because the ICP effect arising from the selective transport of ions in the nanopore^{15,23} becomes significant at low C_{KCl} . In addition, according to eq 8, the nanopore conductance at low C_{KCl} is also significantly affected by σ_w , which can be regulated by the background salt concentration, C_{KCl} , and pH, as will be discussed in detail later. Therefore, the estimated values of $\text{p}K_{\text{A}} = 7$, $\text{p}K_{\text{B}} = 1.9$, and $\Gamma_{\text{total}} = 4.8 \text{ nm}^{-2}$, implying that the isoelectric point (IEP) of the nanopore considered is 2.55, are then used in the following discussions. For illustration, we consider a nanopore with length $L_{\text{N}} = 34 \text{ nm}$ and radius $R_{\text{N}} = 5 \text{ nm}$. A potential bias $V_0 = 200 \text{ mV}$ is applied across the nanopore.

pH-Regulated Nanopore. Figure 3 illustrates the influences of the solution properties, background salt concentration, C_{KCl} , and pH, on the spatial variations of the surface charge density, σ_w , along the inner nanopore wall (a, b) and on the surface-averaged charge density, $\bar{\sigma}_w (= (\int_{\Omega} \sigma_w d\Omega) / \int_{\Omega} d\Omega)$ (c, d), where Ω denotes the surface of the inner nanopore wall. The corresponding spatial variations of the surface concentrations of counterions H^+ (c_{1s}) and K^+ (c_{2s}) along the inner wall of the nanopore for the case of Figure 3a,b are shown in Figure S1 of the Supporting Information. Figure 3 depicts that the magnitude of the nanopore surface charge density, including both $|\sigma_w|$ and $|\bar{\sigma}_w|$, increases with increasing pH and C_{KCl} . The former is expected because the concentration of H^+ ions decreases with increasing pH, leading to more negatively charged SiO^- dissociated from the SiOH functional groups and, therefore, higher negative surface charge density. The latter can be attributed to the excluded effect of K^+ counterions. Since the nanopore wall is negatively charged, both K^+ and H^+ are electrostatically attracted into its surface. However, as the background salt concentration, C_{KCl} , increases, some H^+ ions are expelled from that surface by the increased K^+

ions, resulting in a lower concentration of H^+ ions at the nanopore surface (see Figure S1a,b) and accordingly higher negative surface charge density.

Parts a and b of Figure 3 also depict that σ_w is not a constant and varies spatially along the nanopore wall. The spatial variation of σ_w strongly depends upon the background solution pH. For relatively low pH (pH = 6 in Figure 3a), $|\sigma_w|$ near the cathode side is smaller than that near the anode side. However, if the pH is relatively high (pH = 10 in Figure 3b), that trend is reversed. These behaviors of σ_w can be explained by those of c_{1s} shown in Figure S1a,b of the Supporting Information. For pH = 6 (10), the surface concentration of H^+ , c_{1s} , on the cathode side is higher (lower) than that on the anode side. Higher surface concentration of H^+ near the cathode side (Figure S1a) can be attributed to the ICP effect,²³ resulting in an enrichment (a depletion) of ions near the cathode (anode) side of the negatively charged nanopore. Thus, the surface proton concentration near the cathode side is higher than that near the anode side. However, the occurrence of a higher surface concentration of H^+ ions near the anode side (Figure S1b) has not been theoretically predicted in the literature. As discussed previously, because of the ICP effect, the counterions K^+ and H^+ are enriched (depleted) near the cathode (anode) side of the negatively charged nanopore. However, as shown in Figure 3, the surface charge density of the nanopore increases significantly with an increase in pH. This implies that if the pH (i.e., 10) deviates appreciably from the nanopore's IEP, the surface charge density of the nanopore becomes extremely large and attracts a considerable amount of major counterions (K^+) compacted on the nanopore surface. Combined with the ICP effect, the surface concentration of K^+ ions (c_{2s}) near the cathode side of the nanopore wall is appreciably enriched, resulting in a significant exclusion of minor counterions (H^+) from that surface and, therefore, a lower surface concentration

of H^+ ions (c_{1s}), as shown in Figure S1. These results clearly show that the basic assumption of a constant and position-independent surface charge density on the nanochannel/nanopore^{16,33–41,48,49} is not appropriate, is unrealistic, and may result in an incorrect estimation of ion transport phenomena within the nanopore.

ICP and Axial Local Electric Field. It is generally accepted that the electrokinetic ion transport in a nanopore depends highly on its surface charge density, σ_w ,^{32,33,48,54} which is influenced by the background solution properties (C_{KCl} and pH) and the resulting ICP phenomena. To comprehensively understand the influence of the solution properties on the ICP phenomena in a pH-regulated nanopore, we show the spatial variations of the concentration of net mobile ions ($c_{net} = \sum_{j=1}^4 z_j c_j$) and the axial variations of the cross-section-averaged c_{net} over the nanopore radius for various combinations of the background salt concentration, C_{KCl} , and pH in parts a–c and d, respectively, of Figure 4. The corresponding spatial variations

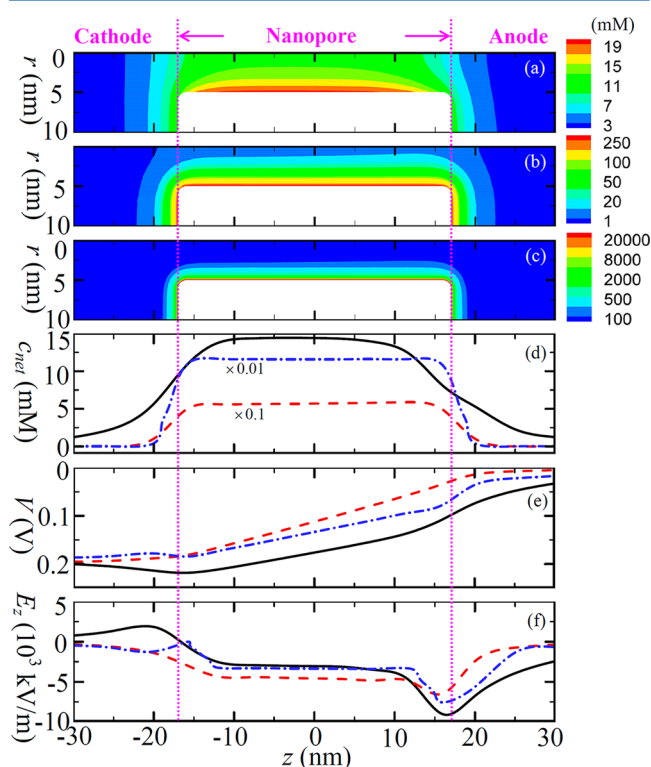


Figure 4. Spatial distributions of the concentrations of net mobile ions, $c_{net} = \sum_{j=1}^4 z_j c_j$ (a–c), and the variations of the cross-section-averaged c_{net} (d), electric potential, V (e), and axial electric field, $E_z = -\partial V/\partial z$ (f), over the nanopore radius for various combinations of the background salt concentration, C_{KCl} , and pH: (a) $C_{KCl} = 1$ mM and pH = 6; (b) $C_{KCl} = 100$ mM and pH = 6; (c) $C_{KCl} = 100$ mM and pH = 10; solid, dashed, and dashed–dotted lines in (d–f) denote the results for (a), (b), and (c), respectively. Scales of 0.1 and 0.01 are applied to the dashed and dashed–dotted lines, respectively, in (d).

of the concentrations of net cations ($c_1 + c_2$) and H^+ ions (c_1) and those of net anions ($c_3 + c_4$) and OH^- ions (c_4) are presented in Figures S2 and S3 of the Supporting Information, respectively. Because the nanopore is negatively charged, more cations are electrostatically attracted into the nanopore, whereas most of the anions are expelled. This phenomenon becomes more appreciable as C_{KCl} and/or the pH increases. In this case, the surface charge density of the nanopore increases

significantly with increasing C_{KCl} and/or pH, resulting in a more considerable amount of counterions (cations) gathered near the nanopore surface and, accordingly, a larger amount of co-ions (anions) repelled out of the nanopore. In addition, the ionic flux of cations (anions) inside the nanopore is significantly larger (smaller) than that in the reservoirs, resulting in an enrichment (a depletion) of concentrations of both ions on the cathode (anode) side of the nanopore, which is the so-called ICP effect as schematically illustrated in Figure 1. Parts a–d of Figure 4 also reveal that the degree of the ICP becomes significant if the C_{KCl} is low or the pH is high. The former is because the smaller the C_{KCl} the more significant EDL overlapping inside the nanopore and, therefore, the more significant the ICP. The latter results from the fact that the nanopore's surface charge density increases with increasing pH, resulting in a greater amount of counterions gathered inside the nanopore (see Figure S2). It is worth noting in Figures S2e and S3e that, due to the ICP effect, both concentrations of H^+ and OH^- ions are significantly enhanced (depleted) near the cathode (anode) side of the nanopore, leading to both pH and pOH gradients along the axis of the nanopore. These results suggest that the simplified PB model to describe the proton concentration in the nanopore with radius comparable to its EDL⁴⁷ is inappropriate and might result in an incorrect estimation.

Parts e and f of Figure 4 show, respectively, the influences of C_{KCl} and pH on the axial variations of the averaged electric potential, V , and axial electric field, $E_z = -\partial V/\partial z$, over the nanopore radius. As expected, the magnitude of the local axial electric field inside the nanopore is much higher than that in the reservoirs, which was consistent with the experimental observation.⁵⁵ Figure 4e reveals that the slope of V versus z is positive for $C_{KCl} = 100$ mM and pH = 6 (dashed line), yielding a negative E_z . On the other hand, the axial electric field is positive in the region near the cathode side of the nanopore for $C_{KCl} = 1$ mM and pH = 6 (solid line) and for $C_{KCl} = 100$ mM and pH = 10 (dashed–dotted line). The positive E_z occurring near the cathode side of the nanopore for the latter two cases can be attributed to a more significant ICP effect as discussed previously. The generated ion concentration gradient across the nanopore induces a local electric field, the direction of which is opposite that of the externally imposed one. The net axial electric field includes the externally imposed one and the induced one by ICP. Since the degree of ICP becomes more significant at lower C_{KCl} , the induced electric field for $C_{KCl} = 1$ mM and pH = 6 is higher than that for $C_{KCl} = 100$ mM and pH = 6. Therefore, the net axial electric field within the nanopore for $C_{KCl} = 1$ mM and pH = 6 (solid line) is lower than that for $C_{KCl} = 100$ mM and pH = 6 (dashed line). Similarly, the net axial electric field inside the nanopore for $C_{KCl} = 100$ mM and pH = 6 (dashed line) is higher than that for $C_{KCl} = 100$ mM and pH = 10 (dashed–dotted line), and this is attributed to a more significant ICP with increasing surface charge density, which increases with pH. It is interesting to note in Figure 4f that the magnitude of the negative E_z is significantly amplified near the anode side of the nanopore, which has also been observed experimentally⁵⁶ and is attributed to significant ion depletion in that region. Therefore, as C_{KCl} decreases or the pH increases, the degree of ICP increases, yielding a more appreciable reversed (enhanced) local electric field occurring near the cathode (anode) side of the nanopore.

Nanopore Conductance and Ion Selectivity. Parts a–d of Figure 5 depict the influences of the background salt

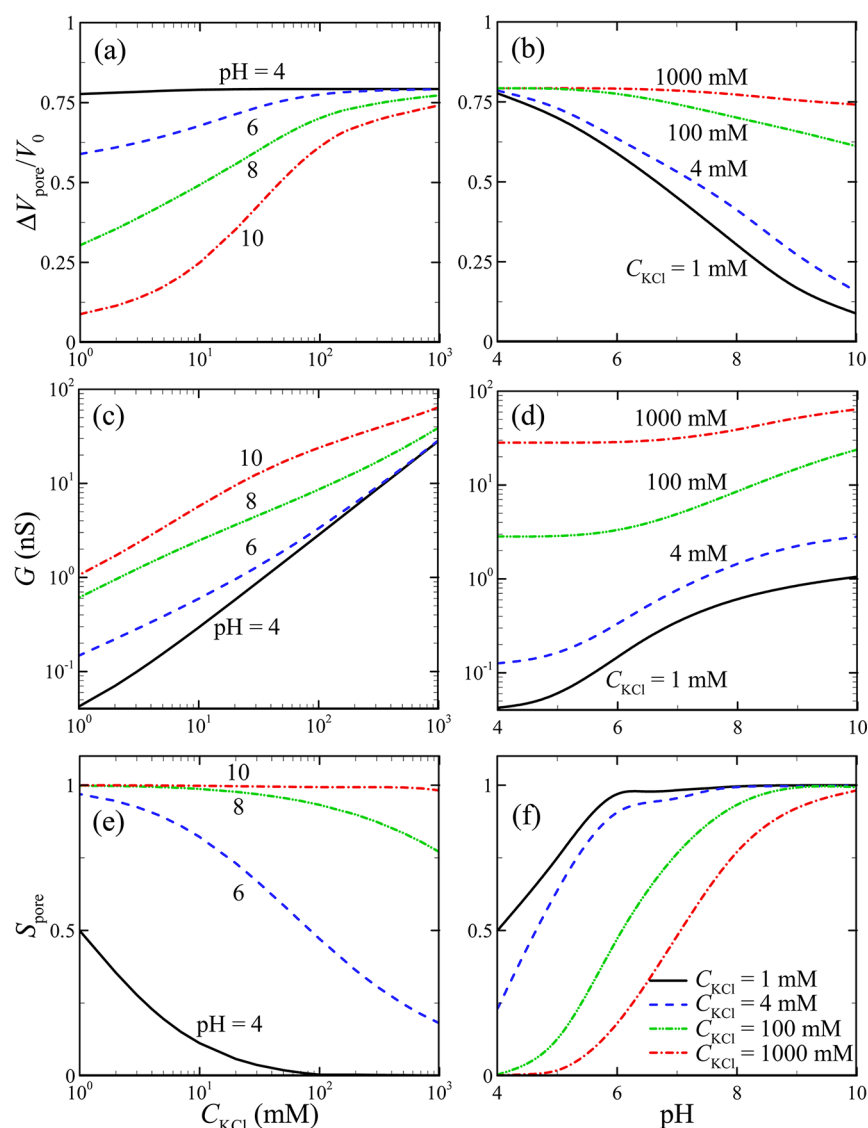


Figure 5. Potential drop, $\Delta V_{\text{pore}}/V_0$ (a, b), conductance, G (c, d), and ion selectivity, S_{pore} (e, f), of the nanopore as a function of the background salt concentration, C_{KCl} , for various background solution pH values (a, c, e) and as a function of pH for various C_{KCl} values (b, d, f).

concentration, C_{KCl} , and pH on the scaled potential drop within the nanopore, $\Delta V_{\text{pore}}/V_0$ (a, b), and the nanopore conductance, G (c, d). The potential drop within the nanopore is obtained from $\Delta V_{\text{pore}} = V(0, L_N/2) - V(0, -L_N/2)$. A larger value of $\Delta V_{\text{pore}}/V_0$ implies that a higher (lower) potential drop and, accordingly, electric field occur inside the nanopore (reservoirs). The local electric field inside the nanopore affects the translocation velocity of sensing entities, while the electric field inside the reservoir affects the capture rate of sensing entities into the nanopore.⁵⁷ In general, the larger the potential drop in the reservoirs, the higher the capture rate. Parts a and b of Figure 5 show that the value of $\Delta V_{\text{pore}}/V_0$ decreases with decreasing C_{KCl} and increasing pH. These behaviors can be attributed to the ICP effect, which becomes significant at low C_{KCl} and/or high pH, as shown in Figure 4.

A significant ICP effect would induce an enrichment (a depletion) of ion concentration near the cathode (anode) side of the nanopore. The generated concentration gradient induces an electric field across the nanopore, the direction of which is opposite that of the externally applied field. Therefore, the net

electric field within the nanopore and accordingly $\Delta V_{\text{pore}}/V_0$ decrease as the degree of ICP increases.

Parts c and d of Figure 5 show that G increases with increasing C_{KCl} and pH. The former is expected, and the latter arises from more counterions accumulated inside the nanopore due to higher surface charge density at higher pH. If C_{KCl} is sufficiently low, G decreases nonlinearly with decreasing C_{KCl} . This stems from the increase in the amount of counterions accumulated inside the nanopore due to a significant EDL overlapping occurring at low C_{KCl} . However, this nonlinear phenomenon becomes insignificant at low pH (i.e., pH = 4 in Figure 5c), which is due to lower surface charge density at lower pH. Figure 5d depicts that the dependence of G on pH at low C_{KCl} is more significant than that at high C_{KCl} . The nanopore conductance is dominated by the bulk ion concentration at high ionic strength and by the effective surface charge of the nanopore at low ionic strength.^{42,58} At low C_{KCl} , the surface charge density of the nanopore increases remarkably with increasing pH, and so does G . On the other hand, if C_{KCl} is relatively high, although the surface charge density also increases with increasing pH, due to the thin EDL

most of the nanopore is occupied by the bulk solution (Figure 4c). Therefore, G increases slightly with increasing pH, as shown in Figure 5d.

Parts e and f of Figure 5 depict the influences of the background salt concentration, C_{KCl} , and pH on the ion selectivity, S_{pore} , of the nanopore, which is the ratio of the difference in currents of counterions and co-ions to the total current, i.e.

$$S_{\text{pore}} = \frac{\sum_{i=1}^N I_{\text{counter}} - \sum I_{\text{co}}}{\sum_{i=1}^N I_i} \quad (9)$$

In general, $S_{\text{pore}} = 1$ and 0 denote a completely cation-selective (or anion-selective) and a nonselective nanopore, respectively. Under the considered conditions, since the nanopore is negatively charged, $\sum I_{\text{counter}} = I_1 + I_2$ from H^+ and K^+ ions and $\sum I_{\text{co}} = I_3 + I_4$ from Cl^- and OH^- ions. As expected, S_{pore} increases with decreasing C_{KCl} , implying that the nanopore becomes more cation-selective. This was consistent with the experimental result of Plecis et al.⁵⁴ and can be attributed to a more significant EDL overlapping inside the nanopore, making co-ions harder to pass through the nanopore. Parts e and f of Figure 5 also reveal that, regardless of C_{KCl} , S_{pore} increases significantly with increasing pH. This can be explained by the fact that the higher the pH the larger the surface charge density of the nanopore and, therefore, the more difficult for the co-ions to flow through it. As a result, if C_{KCl} is low, a lower pH is required to form a completely cation-selective nanopore, as shown in Figure 5f.

CONCLUSIONS

Electrokinetic ion transport in a pH-regulated nanopore was investigated for the first time using a continuum-based model including coupled multi-ion Poisson–Nernst–Planck equations for the ionic mass transport and the Navier–Stokes equations for the flow field. In contrast to the existing studies, where the nanopore is assumed to maintain a constant surface charge density and only two ionic species dissociated from the background salt are considered, the developed model is more general due to the consideration of multiple ionic species and surface equilibrium reactions of dissociable functional groups on the nanopore wall. The developed model predicts that the surface charge density of the nanopore wall becomes spatially dependent, and its prediction on the nanopore conductance agrees well with the experimental data available from the literature. With the verified model, we show that the electric-field-induced ion transport behaviors, such as ICP, ion selectivity, nanopore conductance, and the distributions of the electric potential, the local electric field, and the nanopore's surface charge density, depend highly on the background solution properties such as the pH and salt concentration. The ICP induces an enrichment (depletion) of ions near the cathode (anode) side of the nanopore, and the degree of ICP increases with increasing solution pH and decreasing salt concentration (a more significant EDL overlapping). A significant ICP induces an electric field across the nanopore, the direction of which is opposite that of the externally imposed one. The potential drop and electric field within the nanopore, therefore, decrease with decreasing salt concentration and increasing pH. Due to the ICP effect, it is found that a proton concentration gradient is generated across the nanopore, which in turn results in an asymmetric distribution of the nanopore's surface charge density.

ASSOCIATED CONTENT

Supporting Information

Results of the spatial variations of the surface concentrations of H^+ and K^+ for the case of Figure 3a,b and the influences of the background salt concentration and pH on the spatial variations of the concentrations of net cations and anions and H^+ and OH^- ions for the case of Figure 4. This material is available free of charge via the Internet at <http://pubs.acs.org>.

AUTHOR INFORMATION

Corresponding Author

*Fax: +886-5-5312071 (L.-H.Y.); 757-683-3200 (S.Q.). E-mail: lhyeh@yuntech.edu.tw (L.-H.Y.); sqian@odu.edu (S.Q.).

Notes

The authors declare no competing financial interest.

ACKNOWLEDGMENTS

This work was financially supported by the National Science Council of the Republic of China (Grants NSC 101-2218-E-224-005, NSC-102-2221-E-224-052-MY3, and NSC 102-2218-E-002-006) and NSF Grant DUE-0940895.

REFERENCES

- (1) Li, J. L.; Gershow, M.; Stein, D.; Brandin, E.; Golovchenko, J. A. *Nat. Mater.* **2003**, *2*, 611–615.
- (2) Karnik, R.; Fan, R.; Yue, M.; Li, D. Y.; Yang, P. D.; Majumdar, A. *Nano Lett.* **2005**, *5*, 943–948.
- (3) Dekker, C. *Nat. Nanotechnol.* **2007**, *2*, 209–215.
- (4) Vlassiuk, I.; Kozel, T. R.; Siwy, Z. S. *J. Am. Chem. Soc.* **2009**, *131*, 8211–8220.
- (5) Wanunu, M.; Morrison, W.; Rabin, Y.; Grosberg, A. Y.; Meller, A. *Nat. Nanotechnol.* **2010**, *5*, 160–165.
- (6) Venkatesan, B. M.; Bashir, R. *Nat. Nanotechnol.* **2011**, *6*, 615–624.
- (7) Tsutsui, M.; Hongo, S.; He, Y. H.; Taniguchi, M.; Gemma, N.; Kawai, T. *ACS Nano* **2012**, *6*, 3499–3505.
- (8) Kowalczyk, S. W.; Wells, D. B.; Aksimentiev, A.; Dekker, C. *Nano Lett.* **2012**, *12*, 1038–1044.
- (9) Plesa, C.; Kowalczyk, S. W.; Zinsmeister, R.; Grosberg, A. Y.; Rabin, Y.; Dekker, C. *Nano Lett.* **2013**, *13*, 658–663.
- (10) Lan, W. J.; Holden, D. A.; Zhang, B.; White, H. S. *Anal. Chem.* **2011**, *83*, 3840–3847.
- (11) Zhou, K. M.; Li, L. C.; Tan, Z. N.; Zlotnick, A.; Jacobson, S. C. *J. Am. Chem. Soc.* **2011**, *133*, 1618–1621.
- (12) Vogel, R.; Anderson, W.; Eldridge, J.; Glossop, B.; Willmott, G. *Anal. Chem.* **2012**, *84*, 3125–3131.
- (13) Kozak, D.; Anderson, W.; Vogel, R.; Chen, S.; Antaw, F.; Trau, M. *ACS Nano* **2012**, *6*, 6990–6997.
- (14) Pevarnik, M.; Healy, K.; Toimil-Molares, M. E.; Morrison, A.; Letant, S. E.; Siwy, Z. S. *ACS Nano* **2012**, *6*, 7295–7302.
- (15) Schoch, R. B.; Han, J. Y.; Renaud, P. *Rev. Mod. Phys.* **2008**, *80*, 839–883.
- (16) Vlassiuk, I.; Smirnov, S.; Siwy, Z. *Nano Lett.* **2008**, *8*, 1978–1985.
- (17) Wei, C.; Bard, A. J.; Feldberg, S. W. *Anal. Chem.* **1997**, *69*, 4627–4633.
- (18) Siwy, Z. S. *Adv. Funct. Mater.* **2006**, *16*, 735–746.
- (19) Cheng, L. J.; Guo, L. J. *Chem. Soc. Rev.* **2010**, *39*, 923–938.
- (20) Liu, J.; Kvetny, M.; Feng, J.; Wang, D.; Wu, B.; Brown, W.; Wang, G. *Langmuir* **2012**, *28*, 1588–1595.
- (21) Liu, J.; Wang, D.; Kvetny, M.; Brown, W.; Li, Y.; Wang, G. *Anal. Chem.* **2012**, *84*, 6926–6929.
- (22) Kim, S. J.; Wang, Y. C.; Lee, J. H.; Jang, H.; Han, J. *Phys. Rev. Lett.* **2007**, *99*, 044501.
- (23) Yeh, L. H.; Zhang, M.; Qian, S.; Hsu, J. P.; Tseng, S. J. *Phys. Chem. C* **2012**, *116*, 8672–8677.

- (24) Kwak, R.; Kim, S. J.; Han, J. *Anal. Chem.* **2011**, *83*, 7348–7355.
- (25) Chang, H.; Kosari, F.; Andreadakis, G.; Alam, M. A.; Vasmatazis, G.; Bashir, R. *Nano Lett.* **2004**, *4*, 1551–1556.
- (26) Smeets, R. M. M.; Keyser, U. F.; Krapf, D.; Wu, M. Y.; Dekker, N. H.; Dekker, C. *Nano Lett.* **2006**, *6*, 89–95.
- (27) Das, S.; Dubsky, P.; van den Berg, A.; Eijkel, J. C. T. *Phys. Rev. Lett.* **2012**, *108*, 138101.
- (28) Yeh, L. H.; Zhang, M. K.; Qian, S. Z.; Hsu, J. P. *Nanoscale* **2012**, *4*, 2685–2693.
- (29) Yeh, L. H.; Zhang, M. K.; Joo, S. W.; Qian, S.; Hsu, J. P. *Anal. Chem.* **2012**, *84*, 9615–9622.
- (30) Ali, M.; Ramirez, P.; Mafe, S.; Neumann, R.; Ensinger, W. *ACS Nano* **2009**, *3*, 603–608.
- (31) Lan, W. J.; Holden, D. A.; White, H. S. *J. Am. Chem. Soc.* **2011**, *133*, 13300–13303.
- (32) Guan, W. H.; Fan, R.; Reed, M. A. *Nat. Commun.* **2011**, *2*, 506.
- (33) Daiguji, H.; Yang, P. D.; Majumdar, A. *Nano Lett.* **2004**, *4*, 137–142.
- (34) Cervera, J.; Schiedt, B.; Neumann, R.; Mafe, S.; Ramirez, P. *J. Chem. Phys.* **2006**, *124*, 104706.
- (35) Cheng, L. J.; Guo, L. J. *Nano Lett.* **2007**, *7*, 3165–3171.
- (36) Kubeil, C.; Bund, A. *J. Phys. Chem. C* **2011**, *115*, 7866–7873.
- (37) Ai, Y.; Zhang, M. K.; Joo, S. W.; Cheney, M. A.; Qian, S. *J. Phys. Chem. C* **2010**, *114*, 3883–3890.
- (38) Ai, Y.; Liu, J.; Zhang, B. K.; Qian, S. *Sens. Actuators, B* **2011**, *157*, 742–751.
- (39) Zhang, B. K.; Ai, Y.; Liu, J.; Joo, S. W.; Qian, S. *J. Phys. Chem. C* **2011**, *115*, 24951–24959.
- (40) Singh, K. P.; Kumar, M. *J. Phys. Chem. C* **2011**, *115*, 22917–22924.
- (41) Singh, K. P.; Kumar, M. *Lab Chip* **2012**, *12*, 1332–1339.
- (42) Yeh, L. H.; Zhang, M.; Hu, N.; Joo, S. W.; Qian, S.; Hsu, J. P. *Nanoscale* **2012**, *4*, 5169–5177.
- (43) van der Heyden, F. H. J.; Stein, D.; Dekker, C. *Phys. Rev. Lett.* **2005**, *95*, 116104.
- (44) van der Heyden, F. H. J.; Bonthuis, D. J.; Stein, D.; Meyer, C.; Dekker, C. *Nano Lett.* **2007**, *7*, 1022–1025.
- (45) Andersen, M. B.; Bruus, H.; Bardhan, J. P.; Pennathur, S. *J. Colloid Interface Sci.* **2011**, *360*, 262–271.
- (46) Yeh, L. H.; Xue, S.; Joo, S. W.; Qian, S.; Hsu, J. P. *J. Phys. Chem. C* **2012**, *116*, 4209–4216.
- (47) Chang, C. C.; Kazoe, Y.; Morikawa, K.; Mawatari, K.; Yang, R. J.; Kitamori, T. *Anal. Chem.* **2013**, *85*, 4468–4474.
- (48) Stein, D.; Kruithof, M.; Dekker, C. *Phys. Rev. Lett.* **2004**, *93*, 035901.
- (49) He, Y. H.; Tsutsui, M.; Fan, C.; Taniguchi, M.; Kawai, T. *ACS Nano* **2011**, *5*, 5509–5518.
- (50) Wang, M.; Kang, Q. J.; Ben-Naim, E. *Anal. Chim. Acta* **2010**, *664*, 158–164.
- (51) Qian, S.; Ai, Y. *Electrokinetic Particle Transport in Micro-/Nanofluidics: Direct Numerical Simulation Analysis*; CRC Press: Boca Raton, FL, 2012.
- (52) Yeh, L. H.; Tai, Y. H.; Wang, N.; Hsu, J. P.; Qian, S. *Nanoscale* **2012**, *4*, 7575–7584.
- (53) Yeh, L. H.; Liu, K. L.; Hsu, J. P. *J. Phys. Chem. C* **2012**, *116*, 367–373.
- (54) Plecis, A.; Schoch, R. B.; Renaud, P. *Nano Lett.* **2005**, *5*, 1147–1155.
- (55) Stein, D.; Deurvorst, Z.; van der Heyden, F. H. J.; Koopmans, W. J. A.; Gabel, A.; Dekker, C. *Nano Lett.* **2010**, *10*, 765–772.
- (56) Kim, S. J.; Li, L. D.; Han, J. *Langmuir* **2009**, *25*, 7759–7765.
- (57) He, Y. H.; Tsutsui, M.; Fan, C.; Taniguchi, M.; Kawai, T. *ACS Nano* **2011**, *5*, 8391–8397.
- (58) Schoch, R. B.; Renaud, P. *Appl. Phys. Lett.* **2005**, *86*, 253111.